State Dependence of CO_2 Effective Radiative Forcing from 1/16× to 16×CO_2

IVAN MITEVSKI,[a] LORENZO M. POLVANI,[b,c] HAOZHE HE,[d] GABRIEL A. VECCHI,[a,d] CLARA ORBE,[b,e] BRIAN J. SODEN,[f] AND RON L. MILLER[b,e]

[a] *Department of Geosciences, Princeton University, Princeton, New Jersey*
[b] *Department of Applied Physics and Applied Mathematics, Columbia University, New York, New York*
[c] *Lamont-Doherty Earth Observatory, Columbia University, Palisades, New York*
[d] *High Meadows Environmental Institute, Princeton University, Princeton, New Jersey*
[e] *NASA Goddard Institute for Space Studies, New York, New York*
[f] *Rosenstiel School of Marine, Atmospheric and Earth Science, University of Miami, Miami, Florida*

(Manuscript received 10 July 2024, in final form 7 April 2025, accepted 16 May 2025)

ABSTRACT: Most research on the state dependence of climate sensitivity has focused on radiative feedbacks, with less attention given to radiative forcing. However, recent studies show that the carbon dioxide (CO_2) radiative forcing depends not only on the CO_2 concentration but also on the base state, particularly the stratospheric temperature profile. Hence, we here carry out atmosphere-only experiments with prescribed sea surface temperatures using Community Earth System Model, version 1, Large Ensemble (CESM1-LE), broadband radiative transfer calculations, and a one-dimensional radiative–convective equilibrium model to thoroughly investigate the dependence of effective radiative forcing (ERF) on varying levels of CO_2 forcing and base-state stratospheric temperatures from 1/16× to 16×CO_2. Using both the CESM1-LE and a radiative–convective equilibrium model, we demonstrate that ERF strongly depends on the CO_2 value of the underlying base state, deviating significantly from a simple logarithmic relationship with CO_2 concentration. Specifically, doubling CO_2 from a base state of 8×CO_2 results in an ERF value that is 50% higher than doubling CO_2 from a 1/16×CO_2 state. By decomposing ERF into instantaneous radiative forcing (IRF) and radiative adjustments, we show that the IRF is largely responsible for the state dependence of ERF. We attribute the increase in IRF with CO_2 concentrations to the stratospheric cooling at 10 hPa. Furthermore, we find that the radiative adjustments are not constant with each CO_2 doubling and halving, and their magnitude depends on the method used to compute them, be it via radiative kernels or via offline radiative transfer calculations. A significant implication of our findings is that the state dependence of ERF needs to be taken into account when studying climate sensitivity under large CO_2 perturbations within the feedback-forcing framework.

KEYWORDS: Atmosphere; Forcing; Climate; Greenhouse gases; Radiative forcing

1. Introduction

Estimating equilibrium climate sensitivity (ECS) is a crucial component in understanding the potential impacts of climate change and interpreting the mechanisms of past climate changes. ECS is the global mean surface warming after doubling carbon dioxide (CO_2) concentration from preindustrial (PI) conditions. ECS has been approximated with effective climate sensitivity (EffCS), the surface warming calculated from 150-yr abrupt 4×CO_2 runs and divided by 2, assuming a logarithmic dependence on the radiative forcing with each doubling of CO_2. EffCS is directly proportional to the radiative forcing imposed on the system and inversely proportional to the feedback parameter λ (EffCS = F/λ).

Efforts to determine EffCS have involved various approaches, including the examination of paleoclimatic evidence (Anagnostou et al. 2016, 2020; Farnsworth et al. 2019; Friedrich et al. 2016; Shaffer et al. 2016; Zhu et al. 2019) and modeling studies (Hansen et al. 2005; Bloch-Johnson et al. 2021; Meraner et al. 2013; Mauritsen et al. 2019; Sherwood et al. 2020; Mitevski et al. 2021; Zhu and Poulsen 2020). However, a major assumption in estimating EffCS is that it remains constant under any CO_2 doubling, neglecting the potential for variation due to nonlinear temperature dependence of radiative feedbacks caused by changes in base state and/or CO_2 perturbations (Bloch-Johnson et al. 2021; Sherwood et al. 2015). Additionally, small contributions from nonlogarithmic CO_2-dependent radiative forcing have been reported (Mitevski et al. 2022).

A recent study by He et al. (2023) has provided new insights into the state dependence of ECS, highlighting not only the influence of feedbacks but also the role of the radiative forcing F. The study revealed that the instantaneous radiative forcing (IRF), which constitutes the bulk of F, strongly depends on the climatological base state. Specifically, the IRF increases when computed from a higher CO_2 base state, and this increase is primarily related to the colder stratospheric temperatures associated with higher CO_2 concentrations. These findings align with earlier analytical work (Jeevanjee et al. 2021), emphasizing the importance of stratospheric-surface temperature difference in determining CO_2 IRF. Furthermore, the stratospheric-surface temperature difference was previously shown to explain the spatial and temporal inhomogeneity of the IRF from CO_2 in an Earth system modeling study, despite the CO_2 concentration being uniformly distributed (Huang et al. 2016; Chen et al. 2023).

Most of the previous work on the state dependence of the CO_2 radiative forcing has primarily centered on the IRF (Jeevanjee et al. 2021; He et al. 2023; Pincus et al. 2020), with less attention given to the state dependence of adjustments.

Corresponding author: Ivan Mitevski, mitevski@princeton.edu

DOI: 10.1175/JCLI-D-24-0387.1

Previous studies have emphasized the IRF due to it being better understood (Mlynczak et al. 2016) and significant contribution (around two-thirds) to the effective radiative forcing (ERF), where ERF is the sum of the IRF and the radiative adjustments. Additionally, the IRF has been shown to be the primary driver of the adjustments (Sherwood et al. 2015; Forster et al. 2016; Ramaswamy et al. 2018; Hansen et al. 2005; Smith et al. 2018, 2020a). However, ERF is the most widely adopted definition of radiative forcing (Forster et al. 2016; Ramaswamy et al. 2018; Sherwood et al. 2015) because it has been found to be the most comprehensive measure of its impact on the surface climate (Hansen et al. 2005; Richardson et al. 2019). Hence, the state dependence of ERF in response to CO_2 forcing bears further examination.

Our previous study (Mitevski et al. 2022) demonstrated that ERF exhibits asymmetry across CO_2 doublings and halvings, leading to asymmetric surface temperature responses. Specifically, we found that the ERF increases slightly more than the logarithm of CO_2 concentration, and hence, the temperature response in the CO_2 doubling cases (up to $8\times CO_2$) is stronger than the response in the corresponding CO_2 halvings (down to $1/8\times CO_2$). While other ECS studies have also demonstrated a higher ERF increase than the expected logarithmic dependence (Hansen et al. 2005; Colman and McAvaney 2009; Caballero and Huber 2013), the underlying mechanisms behind this ERF increase, and its decomposition into IRF and adjustments, have yet to be thoroughly explored. To understand this, we here conduct simulations using the Community Earth System Model, version 1, Large Ensemble (CESM1-LE), model, calculating ERF from atmosphere-only experiments with prescribed sea surface temperatures and sea ice starting from different CO_2 base states. Additionally, we carry out offline radiative transfer calculations and use a one-dimensional radiative–convective equilibrium model to calculate IRF. By separately quantifying the IRF and the adjustments, we extend previous work that studied only the state dependence of IRF (He et al. 2023) and elucidate the mechanisms behind the state dependence of ERF. Specifically, we investigate whether the stratospheric temperature response due to a change in CO_2 causes ERF to increase more than the logarithm of the CO_2 concentration and whether the adjustments change as the logarithm of the CO_2 concentration.

2. Methods

a. Models

We utilize the original CESM1-LE (Kay et al. 2015). This model consists of the Community Atmosphere Model, version 5 (CAM5), and the Parallel Ocean Program, version 2 (POP2). The model components have a horizontal resolution of approximately 1°, with 30 vertical levels in the atmospheric model and a model top of 3.6 hPa, and with 60 vertical levels in the ocean model. Additionally, we incorporate some results from the GISS-E2.1-G model (Miller et al. 2021; Kelley et al. 2020). To estimate the IRF from the CESM1-LE runs, we use radiative kernels (Soden et al. 2008) and the radiative transfer model suite of community radiative transfer codes based on Edwards and Slingo (SOCRATES) on monthly model output (Edwards and Slingo 1996; Manners 2015).

To isolate the role of the radiative–convective response in the ERF increase with CO_2, we use a one-dimensional radiative–convective equilibrium model—Konrad (Dacie et al. 2019; Kluft et al. 2019). We run the default configuration of Konrad, which comes with clear skies, fixed relative humidity, fixed ozone, and a saturated isentropic lapse rate in the troposphere. We run Konrad with 100 vertical levels from 1000 to 0.1 hPa. The reference CO_2 concentration is set to 284.7 ppm, the same as in the CESM1-LE experiments. We run Konrad with time steps of 24 h for 150 days. Note that Konrad uses the same radiation code as CESM1-LE, Rapid Radiative Transfer Model for general circulation models (GCMs) (Iacono et al. 2008), to calculate radiative fluxes.

It is important to note that SOCRATES does not use RRTMG for its radiation calculations. Previous work (Pincus et al. 2020) has investigated the differences between SOCRATES and RRTMG and found them to be small. Nonetheless, the use of SOCRATES here contributes some small differences in radiative forcing calculations, compared to CESM1-LE and Konrad, but these do not affect our results or conclusions.

b. Experiments

We conduct 20-yr-long abrupt forcing experiments using the CESM1-LE model with prescribed sea surface temperature and sea ice to preindustrial values, referred to as "prescribed-SST" runs, to examine the effects of stratospheric temperature on the ERF in abrupt CO_2 doublings and halvings. For the doubling experiments, we start from PI conditions and, every 20 years, abruptly double the CO_2 concentration up to $16\times CO_2$ (indicated in red in Fig. 1a). We chose to do the step experiments because the stratospheric temperature adjusts (cools) at each doubling step, allowing us to elucidate its impact on the ERF more cleanly. The halving experiments follow a similar approach; starting from PI conditions, we decrease the CO_2 concentration by half every twenty years. The stratospheric temperature adjusts (warms) at each step, and we continue the steps until $1/16\times CO_2$ (blue in Fig. 1a). Similarly, with Konrad, we first equilibrate to a reference climate, and then, keeping the surface temperature fixed and allowing the atmospheric temperature to adjust, we perturb the CO_2 concentration from $1/16\times$ to $16\times CO_2$.

c. ERF

The ERF in the CESM1-LE runs is calculated as the global mean net top-of-the-atmosphere (TOA) radiation between two adjacent CO_2 steps, incorporating both stratospheric and tropospheric adjustments (Sherwood et al. 2015). While the SSTs and sea ice concentrations (SICs) are fixed at PI values, the land temperature in CESM1-LE responds to the radiative forcing, as prescribing fixed land surface conditions in a climate model presents technical challenges (Andrews et al. 2021; Hansen et al. 2005; Ackerley et al. 2018). The land warms and cools with increasing and decreasing CO_2 levels, respectively. This land surface temperature response introduces a radiative effect and some adjustments, which we separately quantify as

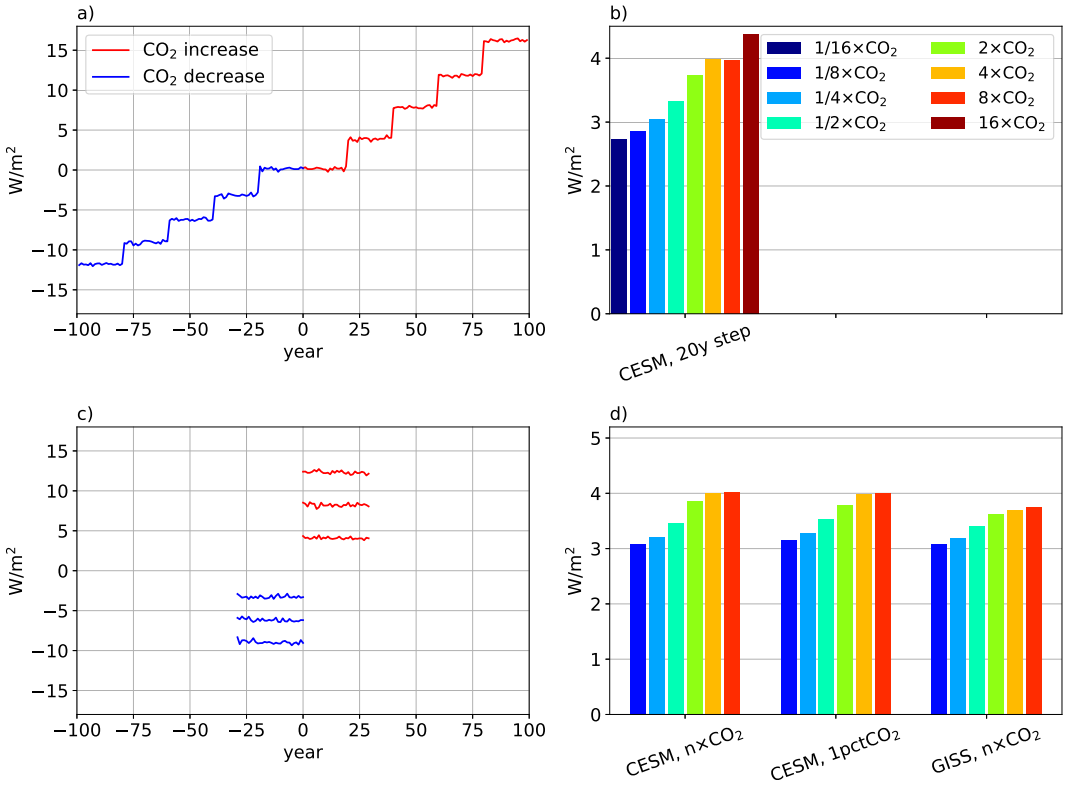

FIG. 1. (a) The radiative imbalance at the TOA in the 20-yr step experiments with CESM1-LE, where CO_2 is doubled (red) or halved (blue) starting from the PI condition (years from −20 to 20). (b) The ERF, calculated as the difference between the two levels shown in (a). (c) The radiative imbalance at the TOA in the $n\times CO_2$ prescribed-SST runs, starting from the PI CO_2 concentration [distinct from the step experiments in (a) and (b), previously documented in Mitevski et al. (2022)]. (d) Normalized ERF (divided by $\log_2 n$) obtained from the (left) abrupt $n\times CO_2$ run with CESM1-LE, (center) 1pctCO2 runs with CESM1-LE, and (right) abrupt $n\times CO_2$ runs with the GISS-E2.1-G model, with adjustments made for land warming, previously documented in Mitevski et al. (2022).

surface temperature adjustment A_{T_s} by multiplying the surface temperature radiative kernel with the surface temperature. Since the surface temperature is fixed in Konrad, we simply compute the ERF as the difference in net TOA radiation between each successive CO_2 doubling/halving run.

d. IRF and adjustments

To calculate the IRF, we employ two different approaches. First, using the double call method, we estimate the IRF using offline radiative transfer calculations with the SOCRATES broadband model (Edwards and Slingo 1996; Manners 2015). In the double call method, we first compute the net TOA radiative flux using SOCRATES with the initial atmospheric state. We then repeat the computation with a perturbed CO_2 concentration (e.g., doubled) and find the IRF as the difference in the net TOA radiative flux. We do these calculations twice, once as a forward calculation with the unperturbed atmospheric state from each CO_2 level and doubled the CO_2 concentration and second as a backward calculation with the perturbed atmospheric state for each CO_2 level and keeping the CO_2 concentration the same. We then take the average of both forward and backward calculations to find the IRF. Nonetheless, the forward and backward calculations yield similar results.

Second, we estimate IRF as a residual by subtracting the rapid adjustments from the ERF. Rapid adjustments occur on a much shorter time scale than the radiative feedbacks and are decoupled from the surface response. Following the approach of Soden et al. (2008), we express the ERF resulting from a climate perturbation as a sum of IRF and several rapid adjustments:

$$\mathrm{ERF} = \mathrm{IRF} + A_T + A_{T_s} + A_q + A_\alpha + A_c, \qquad (1)$$

where A_x are the rapid adjustments, x is the atmospheric temperature T, T_s is the surface temperature, q is the specific humidity, α is the surface albedo, and c represents the clouds. We further separate the rapid adjustments into stratospheric and tropospheric contributions using a tropopause that varies linearly from 100 hPa at the equator to 300 hPa at the poles. The radiative kernel K_x approximates the change in TOA shortwave or longwave radiation ΔR resulting from a unit change in the state variable Δx, such that $K_x \approx \partial R/\partial x$ and $A_x = K_x \Delta x$. The cloud kernels A_c are determined following the method of Soden et al. (2008) by computing the difference

between all-sky kernel decomposition and clear-sky kernel decomposition. The radiative kernels are calculated by making small perturbations in the model's base climatology and running the resulting atmosphere through an offline radiative transfer code. TOA fluxes were then compared between the perturbed and base states. Since stratospheric adjustments have been shown to depend on the vertical resolution of the kernel (Smith et al. 2020b), we perform adjustment calculations using three different kernels that have the highest pressure level of 1 hPa or more from the following models: HadGEM3-GA7.1 (Smith et al. 2020a), ECMWF-RRTM (Huang et al. 2017), and ECHAM6 (Block and Mauritsen 2013). The results in all figures represent the mean of these three kernels. While the kernel method offers advantages for computing adjustments—such as eliminating the need to run offline radiative transfer models and enabling easier decomposition of individual adjustments—it also introduces uncertainties. These include the choice of the kernel base state, the kernel model top, and, most importantly, the linearity of the kernel, particularly when exploring adjustments at very high or low CO_2 concentrations. A more detailed discussion of these uncertainties, along with a comparison of adjustment computations using kernels versus offline calculations with SOCRATES, is provided later in the text.

We calculate the stratospheric adjustment with SOCRATES by doing two offline calculations with the same CO_2 concentrations but a different atmospheric state (e.g., temperature profile). In the Konrad simulations, we calculate the adjustments simply as a residual between the ERF and the IRF.

3. Results

a. *Nonlogarithmic ERF increase with CO_2 concentrations*

We start with the step experiments with CESM1-LE (Fig. 1a) where CO_2 is increased from PI to $16\times CO_2$ values in 20-yr steps (red) and similarly decreased to $1/16\times CO_2$ (blue). We calculate the resulting ERF as the difference between two consecutive CO_2 steps. While a purely logarithmic relationship would imply equal ERF for each step, we observe that the absolute value of the "blue step" at year −80 is considerably smaller than the absolute value of the "red step" at year 80. Figure 1b displays the calculated ERF from each step, revealing that the ERF does not remain constant but increases more than the expected logarithmic dependence of the CO_2 concentration, with the ERF from CO_2 doubling rising from 2.8 W m^{-2} at $1/16\times CO_2$ to 4.5 W m^{-2} at $8\times CO_2$.

In our previous work (Mitevski et al. 2021, 2022), we calculated the ERF from abrupt $n\times CO_2$ forcing (from $1/8\times$ to $8\times CO_2$) as the net TOA radiation between the $n\times CO_2$ states and PI, which we reproduce those results here in Fig. 1c, for the sake of completeness. The ERF calculated this way with the same CESM1-LE model (Fig. 1d) exhibits an increase larger than the logarithmic relationship with CO_2 concentration. Specifically, the ERF increases from 3 W m^{-2} at $1/8\times CO_2$ to 4 W m^{-2} at $8\times CO_2$. Note that these experiments differ from the 20-yr step experiments in Figs. 1a and 1b in that they always start from the PI atmospheric state and yet yield similar ERF increases with CO_2. Furthermore, we obtain similar results with

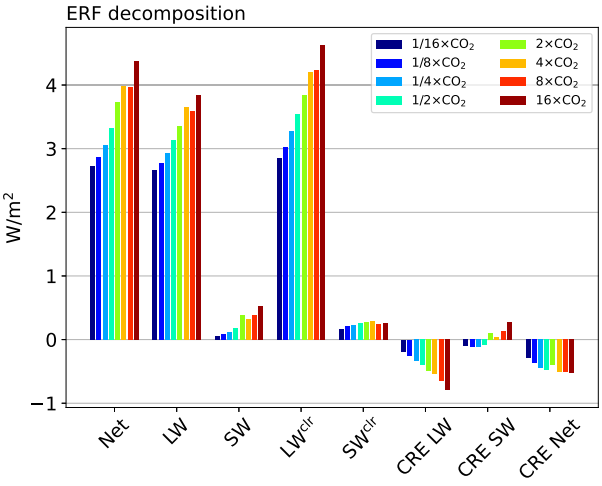

FIG. 2. Net TOA radiation for the runs in Figs. 1a and 1b decomposed into LW, SW, all sky, clear sky (clr), and CREs. CRE is the difference between all sky and clear sky.

increasing and decreasing CO_2 by $1\%yr^{-1}$ (1pctCO2 runs) with CESM1-LE and abrupt $n\times CO_2$ runs with the GISS model (Fig. 1d). These ERF increases exceed both the logarithmic relationship and the simplified expressions proposed in the literature (Byrne and Goldblatt 2014; Etminan et al. 2016) (see Fig. 2 in Mitevski et al. 2022). The similarity between the abrupt $n\times CO_2$, the 20-yr abrupt step, and $1\%yr^{-1}$ CO_2 forcing experiments demonstrates that the ERF increase with CO_2 concentration is independent of the method used to perturb CO_2 in prescribed-SST runs with a general circulation model. Furthermore, the GISS-E2.1-G model results confirm that the ERF increase is not limited to a particular model—we hypothesize that the result will be found in other GCMs. Last, our findings indicate that the ERF increases with CO_2 irrespective of whether we start from the PI or an $n\times CO_2$ atmospheric state.

Next, we decompose the net TOA radiation imbalance (which, by definition, is the ERF) in the "step" experiments from Fig. 1b into longwave (LW) and shortwave (SW) components, as well as the clear sky (clr), all sky, and cloud radiative effects (CREs) in Fig. 2. As one would expect, most of the increase in net TOA radiation with CO_2 comes from the all-sky LW component (second set of bars), with a smaller contribution from the SW all-sky component. Further decomposition of the LW component shows that most of the increase with CO_2 comes from the clear-sky LW, with the CRE LW opposing the rise. We find that the net CRE (CRE Net) has a relatively small impact on the overall ERF increase, and it actually opposes the ERF increase.

More importantly, we find that the nonlogarithmic ERF increase with CO_2 concentration coincides with an increase in the IRF (Fig. 3). First, we compute the IRF (Fig. 3a) as the residual between the ERF and the total adjustments, which in turn are calculated with radiative kernels (see methods). Our analysis reveals that the IRF, calculated as a residual, increases with CO_2, particularly showing a pronounced increase between

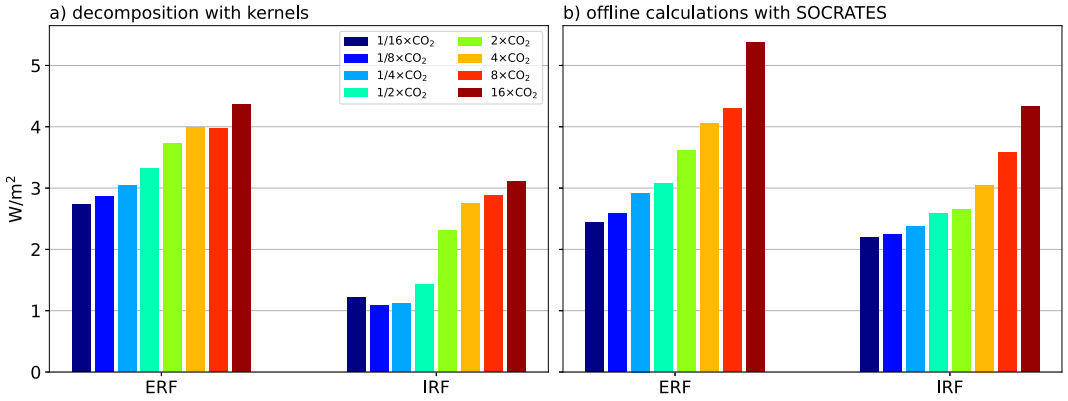

FIG. 3. ERF and IRF with (a) kernel decomposition and (b) offline calculations with SOCRATES.

1/2× and 2×CO_2. In addition, we carry out offline radiative transfer calculations with SOCRATES using the same atmospheric profiles from the 20-yr step experiments to compute both ERF and IRF (Fig. 3b). These radiative transfer calculations confirm our findings with the CESM1 prescribed-SST runs and clearly show a similar monotonic increase from 1/16×CO_2 to 16×CO_2. The ERF increase here also corresponds with the IRF's increase, although the IRF has a more gradual increase from 1/16×CO_2 to 16×CO_2 with no step-like behavior between 1/2× and 2×CO_2 like the IRF calculated as a residual in Fig. 3a. In the next section, we investigate the IRF discrepancy between both calculations.

The IRF's state dependence, specifically its increase with CO_2, has been investigated in prior studies (Huang et al. 2016; Jeevanjee et al. 2021; He et al. 2023; Chen et al. 2024), which have demonstrated that the emission temperatures within the troposphere and stratosphere can account for the IRF's state dependence. Specifically, when the surface temperature is fixed, a decrease in stratospheric temperature is anticipated to correspond with an increase in IRF. In our experimental setup with CESM1-LE, we vary CO_2 concentrations from 1/16× to 16×CO_2, consequently altering the stratospheric temperature near CO_2 emissions (near 10 hPa, T_{10hPa}) from 260 to 205 K, while the near-surface temperature responds very little compared to T_{10hPa} (see Fig. 4a). It is well established in the literature that the addition of CO_2 leads to surface and tropospheric warming but induces stratospheric cooling (Manabe and Wetherald 1967; Ramaswamy et al. 2006). The opposite occurs when CO_2 is removed: The surface and troposphere cool, while the stratosphere warms. Hence, we analyze the relationship between T_{10hPa} and ERF, and consistent with the previous literature, we find a strong negative correlation ($R^2 = 0.99$) in Fig. 4b. As the stratospheric temperatures decrease, ERF increases. Moreover, whether the IRF is computed directly with SOCRATES or indirectly as a residual, its correlations with T_{10hPa}, $R^2 = 0.81$, and $R^2 = 0.95$, are very high. Therefore, we conclude that the IRF increase with CO_2 associated with stratospheric cooling near 10 hPa largely explains the observed rise in ERF. This direct link between stratospheric temperature states and the increase in ERF largely explains the state dependence of ERF on CO_2 concentration.

b. *Nonlogarithmic CO_2 dependence of radiative adjustments*

To gain further insight into the difference in IRF values when calculated from SOCRATES or from the kernels shown in Fig. 3, we now consider the radiative adjustments in Fig. 5. The total of the adjustments calculated from the kernels $\sum_i A_i$

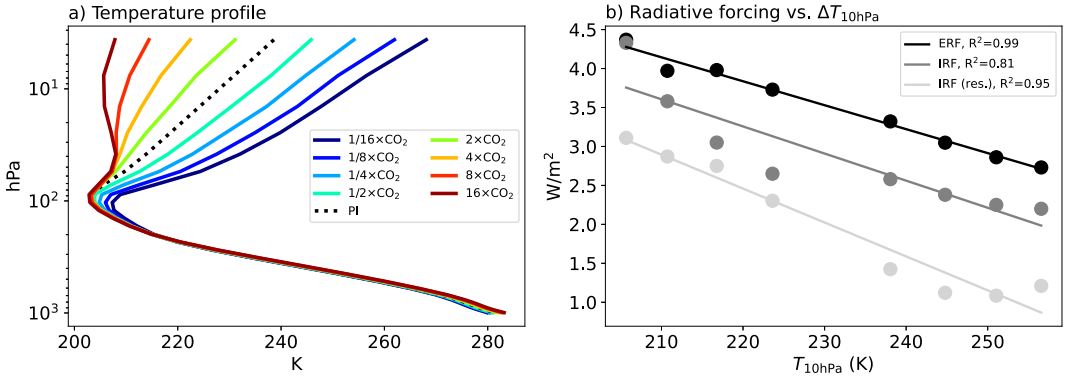

FIG. 4. (a) Global mean atmospheric temperature profiles for the 20-yr step experiments from Fig. 1a. (b) ERF, IRF calculated from SOCRATES (IRF), and IRF calculated as a residual from the kernel adjustment calculations IRF (res.) on the *y* axis correlated with temperature response at 10 hPa on the *x* axis.

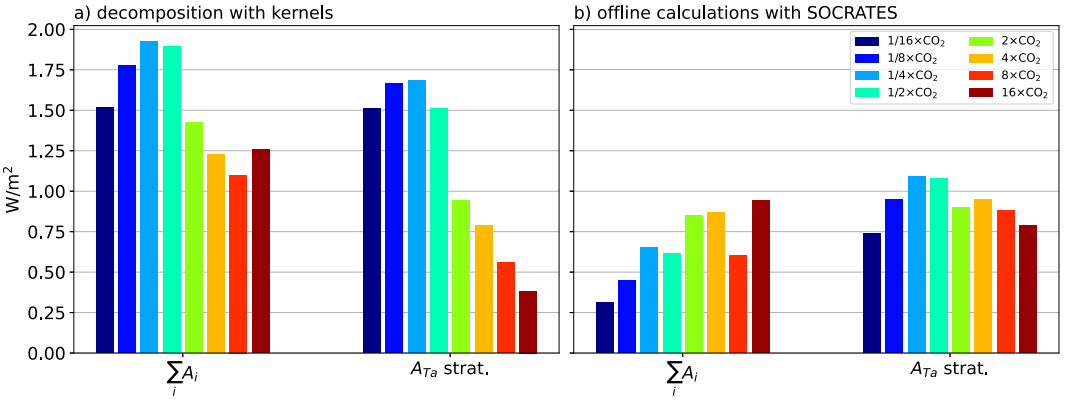

FIG. 5. Total adjustments $\sum_i A_i$ and stratospheric temperature adjustments A_{T_a} strat. calculated with (a) kernels and (b) offline radiative transfer calculations with SOCRATES.

(Fig. 5a) is found to be much larger in the cases with decreasing CO_2 levels compared to those with increasing CO_2 levels, resulting in an overall decreasing but nonmonotonic dependence with CO_2 concentration. This decrease with CO_2 concentration, which is largest between 1/2× and 2×CO_2, explains why the IRF calculated as the residual increases the most between 1/2× and 2×CO_2. Additionally, we compute the adjustments using offline calculations with SOCRATES (Fig. 5b; also see methods) and find that the total adjustments increase nonmonotonically with CO_2, which is opposite to what we find with the kernel calculations. Although both SOCRATES and the kernel method show nonconstant adjustments, they exhibit opposite overall changes from 1/16× to 16×CO_2. Therefore, caution is needed when studying the adjustments across multiple CO_2 doublings and halvings using the kernel method.

An important caveat regarding the kernel calculations is that kernels are derived for small perturbations in warming scenarios and do not account for any state dependency, as reported by previous studies (Jonko et al. 2012), which likely has an impact on the wide CO_2 range we explore here. To check for any state dependency in the kernel calculations, we repeat the adjustment calculations with offline radiative transfer calculations with SOCRATES. The SOCRATES calculations exhibit some similarities with the kernel calculations (Fig. 5): Total adjustments increase between 1/16× and 1/2×CO_2 and decrease between 2× and 8×CO_2, while showing an increase at 16×CO_2. The change in stratospheric adjustment largely follows this pattern from 1/16× to 1/2×CO_2. The largest difference between kernels and SOCRATES calculations occurs between 1/2× and 2×CO_2, where there is a large decrease of almost 0.5 W m^{-2} in the kernel calculations, likely attributable to state dependence. Further exploration of the state dependence of kernels, particularly in CO_2 decrease scenarios, is clearly needed but lies beyond the scope of our work here.

Surprisingly, we find that the stratospheric adjustment is not constant with each CO_2 doubling/halving perturbation calculated with both kernels and SOCRATES, with the strongest response when calculated with kernels (Fig. 5a). Since the stratospheric temperature adjustment is simply the spatial and vertically integrated product between the stratospheric temperature response and the radiative kernel, we can further clarify whether the temperature response or the radiative kernel itself causes the stratospheric adjustment to not be constant with each CO_2 doubling/halving. Since the kernels are constant across all the CO_2 perturbations, they do not impact the stratospheric adjustment across CO_2 levels. In fact, we find that the stratospheric temperature response has a stronger response when CO_2 concentration is lower (e.g., 1/4×CO_2) and monotonically increases with CO_2 up to 16×CO_2 (Fig. 6). Hence, the temperature response explains the asymmetry in the stratospheric adjustment (A_{T_a} strat. in Fig. 5a): It increases between 1/16× and 1/4×CO_2 and then decreases up to 8×CO_2.

One possible explanation for the stronger stratospheric temperature response in the CO_2 decrease cases compared to the CO_2 increase cases (Fig. 6) is the anticipated changes in emissivity at different CO_2 levels. Emissivity is directly proportional to the CO_2 concentration (Hartmann 2015), so it is smaller for the CO_2 decrease cases and larger for the CO_2 increase cases up to 16×CO_2. Hence, owing to the higher emissivity in the CO_2 increase scenarios (assuming a constant radiative flux divergence in the stratosphere with each CO_2 perturbation), a smaller stratospheric cooling is enough to restore radiative equilibrium in the stratosphere. The opposite occurs when lowering CO_2 concentrations, when a larger stratospheric temperature change is needed to reestablish radiative equilibrium. The qualitative dependence of emissivity on CO_2 concentration at least accounts for the sign of the change in the stratospheric temperature adjustment: a stronger temperature response at low CO_2 values to compensate for the low emissivity and a weaker temperature response at high CO_2 levels. However, because stratospheric temperature is itself a state-dependent variable that influences radiative flux divergence, it could potentially offset the impact of emissivity changes. Nonetheless, a more detailed investigation, including a careful examination of the role of the vertical lapse rate and a thorough analysis of the spectral structure, is necessary to fully comprehend the nonconstant adjustments. However, these lie beyond the scope of our work here.

Another possible explanation for why the stratospheric temperature response in the CO_2 decrease cases is stronger

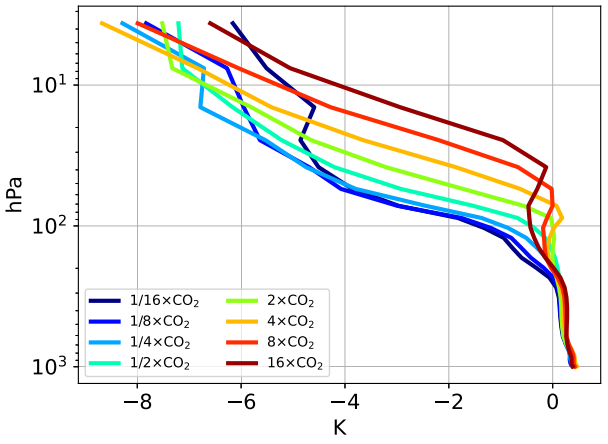

FIG. 6. Stratospheric temperature response between each successive CO_2 doubling and halving in the 20-yr step experiments from Fig. 1a.

than in the CO_2 increase cases is the change in the pressure of the emission level. In a previous study by Jeevanjee et al. (2021), the emission pressure level was found to be inversely proportional to the CO_2 concentration. Therefore, with each CO_2 doubling, the emission pressure level shifts below 10 hPa, effectively raising the stratospheric temperature profile (Fig. 6), while the stratospheric lapse rate remains unchanged. Similarly, with each CO_2 halving, the emission pressure level shifts above 10 hPa, thereby lowering the stratospheric temperature profile (Fig. 6). Hence, from the shift in emission pressure level, when integrating over the stratosphere, we can deduce a stronger stratospheric temperature response upon halving than upon doubling CO_2 (see schematic in Fig. A1 in the appendix).

We further decompose the total adjustments $\sum_i A_i$ into the individual adjustments (Fig. A2) and find that the largest contribution comes from the stratospheric temperature adjustment (A_{T_a} strat.), while the tropospheric adjustments predominantly exhibit negative values and do not contribute to the overall $\sum_i A_i$ decrease with CO_2. Furthermore, within the stratospheric adjustments, the temperature response is the primary driver, with minimal contributions from stratospheric water vapor in the longwave and shortwave. Regarding the tropospheric adjustments, the largest contribution to the increase in ERF with CO_2 is the cloud adjustment A_c; however, the tropospheric temperature adjustment A_{T_a} trop. opposes it (Fig. A2).

c. *Results with an radiative–convective equilibrium (RCE) model*

The stratospheric temperature response to CO_2 doubling/halving is due to radiative, convective, and large-scale circulation adjustments (Wang and Huang 2020). In the CESM1-LE calculations, sea surface temperatures remain fixed, allowing radiative, convective, and atmospheric circulation to adjust at each $n\times CO_2$ level. Given the potential impact of circulation adjustment on the stratospheric temperature, it is crucial to isolate this effect to determine its significance for the stratospheric temperature response. To separate the influence of stratospheric dynamics on temperature adjustment, we utilize a one-dimensional radiative–convective equilibrium model, Konrad (see methods). Since Konrad lacks any horizontal circulation (and thus any adjustment thereof), it allows us to isolate the radiative–convective response in the increase in ERF with CO_2. We find that ERF calculated with Konrad also increases from 1/16× to 16×CO_2: from 3.2 to 5.1 W m^{-2} (Fig. 7a), further corroborating our previous results with CESM1-LE (Fig. 3). Furthermore, we find that the IRF calculation with Konrad is also the primary driver of the ERF increase, consistent with CESM1-LE. Konrad also produces a similar response in the total adjustments as the SOCRATES calculations from CESM1-LE model output: an increase from 1/16× to 1/2×CO_2 and a decrease from 2× to 16×CO_2 ($\sum_i A_i$ in Fig. 7a). Last, we find that Konrad exhibits the same stratospheric temperature response as the CESM1-LE model: higher response at low CO_2 values and weaker response at high CO_2 values (Figs. 7b,c). Hence, the agreement between CESM1-LE and Konrad leads us to conclude that the adjustment of the stratospheric circulation is unlikely to play an important role in determining the ERF dependence on CO_2.[1] Moreover, the consistency in the response of the total adjustments between offline calculations with SOCRATES (based on CESM1-LE data) and on the 1D Konrad simulations, in spite of the different broadband radiation codes, indicates that our findings are robust and likely not radiation model dependent.

4. Discussion and conclusions

We have investigated the state dependence of effective radiative forcing (ERF) using prescribed-SST runs with Earth System Model CESM1-LE and the radiative–convective equilibrium model Konrad. We have found that ERF increases by over 50% more than the value expected from the logarithmic dependence on CO_2 concentration in the range from 1/16× to 16×CO_2. We have decomposed the ERF into instantaneous radiative forcing (IRF) and adjustments and attributed the ERF increase primarily to an increase in IRF. This increase in clear-sky IRF, in turn, was linked to the cooling of stratospheric temperatures with increasing CO_2 concentration. Furthermore, we have found a nonconstant stratospheric temperature adjustment across CO_2 perturbations, with larger temperature responses at lower CO_2 values and smaller responses at higher CO_2 values. We do not currently have a simple and compelling explanation for why the stratospheric temperature response has a larger magnitude at low CO_2 concentrations, but we suggest that this tendency arises from changes in emissivity and emission pressure as CO_2 concentration rises from 1/16× to 16×CO_2. However, a more rigorous attribution should also consider the spectral variations of the radiative forcing.

It is important to note that our IRF calculations for CESM1-LE using SOCRATES were performed using the

[1] One caveat is worth noting: CESM1-LE is a notoriously low-top model, and its representation of the Brewer–Dobson circulation is probably quite biased. It would thus be valuable to confirm (or possibly invalidate) our conclusion with a high-top model with realistic Brewer–Dobson circulation.

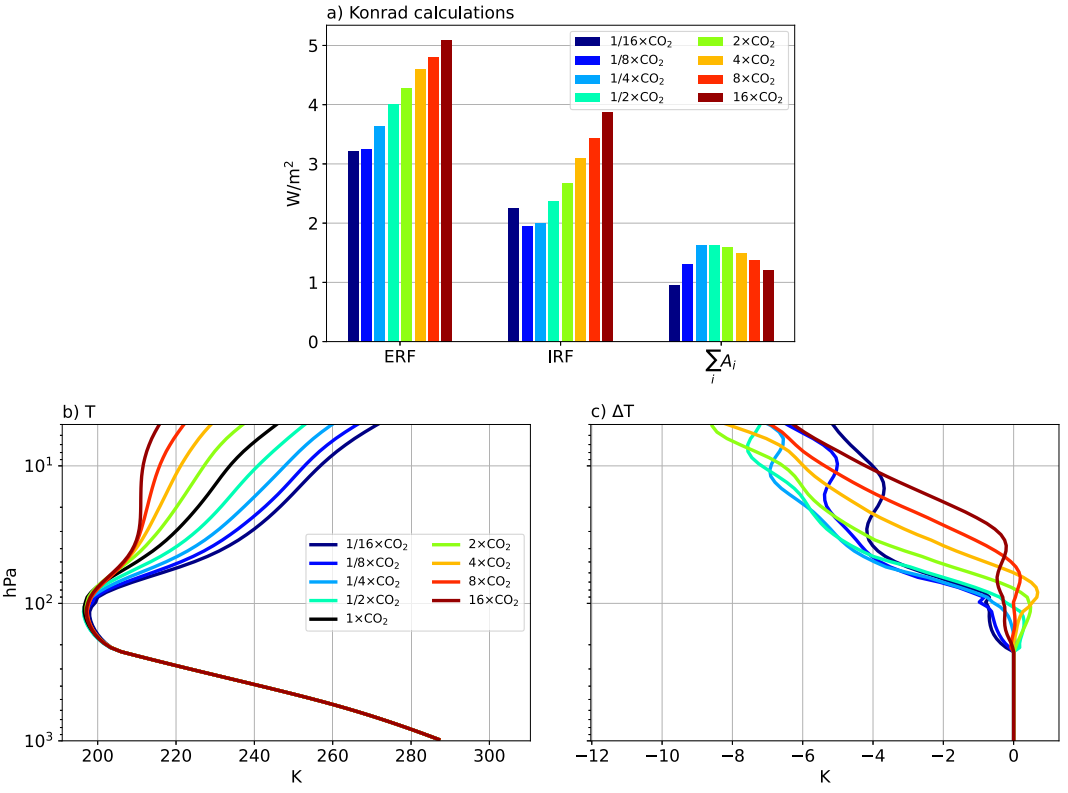

FIG. 7. Results with one-dimensional RCE model Konrad for (a) ERF decomposition into IRF and adjustments, (b) temperature profiles, and (c) temperature response per CO_2 doubling.

base state corresponding to $n\times CO_2$. As a result, the nonlogarithmic behavior of IRF was attributed to changes in the atmospheric state, primarily the stratospheric temperature, in each $n\times CO_2$ run, along with the change in CO_2 concentration. By doubling the CO_2 concentration from each $n\times CO_2$ base state, we did not specifically explore the extent to which IRF depends solely on the CO_2 forcing. To isolate the importance of the CO_2 concentration from changes in the base state, we additionally calculate IRF with Konrad while maintaining the base state at $1\times CO_2$ and only perturbing the CO_2 concentration from $1/16\times$ to $16\times CO_2$. Comparing this with IRF calculated starting from different $n\times CO_2$ states (Fig. 8), we find that IRF remains nearly constant when computed from the same $1\times CO_2$ base state (the second set of bars in Fig. 8) compared to when computed by doubling CO_2 from $n\times CO_2$ state (the first set of bars in Fig. 8). Hence, the majority of the IRF increase stems not from the actual CO_2 concentration but from the base state at which it is computed. The negligible impact of the CO_2 concentration compared to the base state has been noted by other studies (He et al. 2023; Pincus et al. 2020).

One limitation to our adjustment calculations for CESM1-LE (Fig. 6) is the uncertainty arising from the choice of kernel base state, kernel model top, and kernel linearity at very high/low CO_2 perturbations. First, Pincus et al. (2020) demonstrated that radiative transfer calculations across different line-by-line models yield consistent results when performed on an identical base state. Therefore, the base state is the primary source of uncertainty across different line-by-line models, and this base-state dependence is also critical for kernel calculations. By performing calculations with three different kernels, we attempt to estimate this uncertainty (Fig. A2). Second, the uncertainty across kernels is also caused by the different model tops, as described in Smith et al. (2020b). Variations in stratospheric adjustments derived from kernels can exhibit nearly a twofold difference, as depicted in Fig. 5 of Smith et al. (2020b). Third, the kernel method relies on the assumption of linearity between top-of-the-atmosphere (TOA)

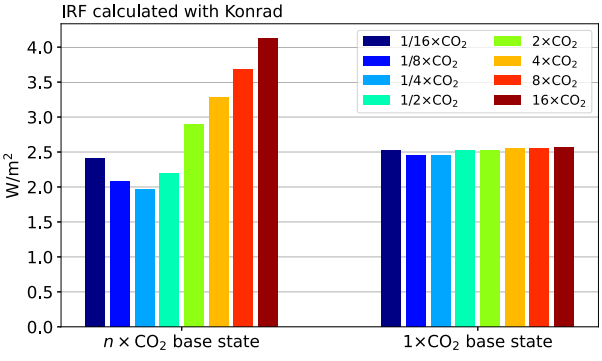

FIG. 8. Normalized clear-sky IRF (divided by $\log_2 n$) calculations using base state of each (left bars) $n\times CO_2$ run (same as IRF in Fig. 7a) and (right bars) $1\times CO_2$ base state.

radiative fluxes and atmospheric variables. However, this linearity assumption is limited to small climate perturbations and may break down under higher forcing scenarios (e.g., 16×CO_2), as shown by Jonko et al. (2012), particularly when CO_2 levels are decreasing, as we found between the 1/2× and 2×CO_2 in our calculations (Fig. 5a). Hence, these issues ought to be taken into account when utilizing kernels to quantify adjustments.

An additional limitation of our experiments is the absence of fixed land temperatures. Land warming/cooling has the potential to induce feedbacks and alter the atmospheric circulation, which, in turn, can impact cloud adjustment. We can incorporate the surface temperature adjustments calculated from kernels to address this issue. However, we find that the adjustment due to land surface temperatures is roughly constant across the CO_2 experiments and does not impact the ERF increase (A_{T_s}, Fig. A2). In addition, our results with CESM1-LE are clearly corroborated by the results from Konrad, which lacks land surface interactions, indicating that our findings are not sensitive to the radiative adjustment due to land temperature response.

Our key finding, that ERF is larger at larger CO_2 concentrations, underscores the importance of carefully considering radiative forcing when studying the response of the climate system to increases in CO_2. Furthermore, our results demonstrate that the radiative adjustments can also vary considerably with different CO_2 forcings. Thus, when studying the state dependence of CO_2's forcing, it is crucial not only to calculate the IRF but also to incorporate the adjustments and compute the entire ERF.

Acknowledgments. Without implying their endorsement, we thank Nadir Jeevanjee and Robert Pincus for helpful discussions at various points during the course of this work. Part of the computing and data storage resources, including the Cheyenne supercomputer (https://doi.org/10.5065/D6RX99HX), were provided by the Computational and Information Systems Laboratory at the National Center for Atmospheric Research (NCAR). IM was supported by a Harry Hess postdoctoral fellowship from Princeton Geosciences. LMP is grateful to the U.S. National Science Foundation for its continued support under Award 2335762.

Data availability statement. The experiments with CESM1-LE and GISS-E2.1-G models were previously analyzed in Mitevski et al. (2021, 2022, 2023). The CESM1-LE model data can be obtained at https://doi.org/10.5281/zenodo.5725084, and the GISS-E2.1-G model data can be obtained at https://doi.org/10.5281/zenodo.3901624.

APPENDIX

Figures A1 and A2 are supplementary figures to the main text.

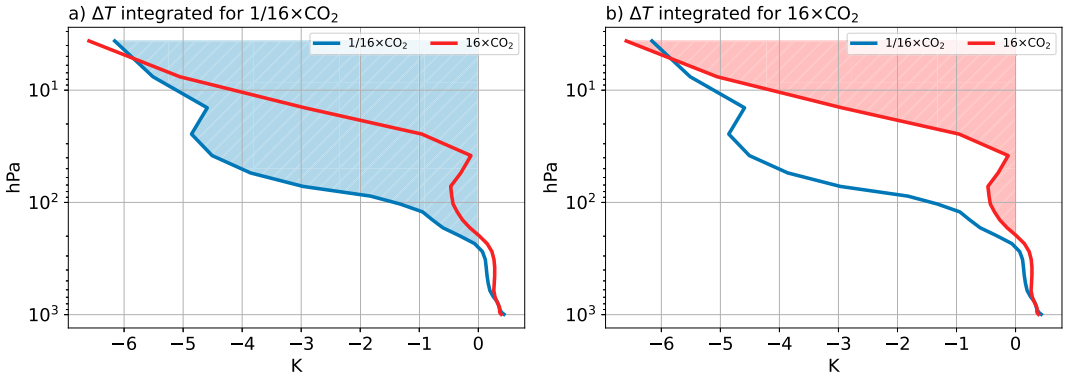

FIG. A1. Schematic of integrating the temperature response profile from (a) 1/16×CO_2 (blue) and (b) 16×CO_2 (red). The stratospheric temperature response associated with CO_2 halving between 1/16× and 1/8×CO_2 is shown in the blue line, and CO_2 doubling between 8× and 16×CO_2 in the red line from the 20-yr step experiments (same as in Fig. 6).

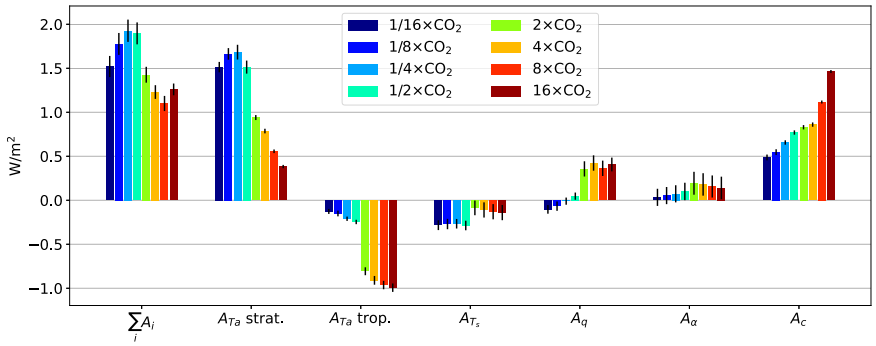

FIG. A2. Total radiative adjustments $\sum_i A_i$ decomposed into stratospheric temperature (A_{T_a} strat.), tropospheric temperature (A_{T_a} trop.), surface temperature (A_{T_s}), water vapor (A_q), albedo (A_α), and cloud (A_c) adjustments. The vertical lines show one standard deviation of the three kernels, and the bars show the mean. See the methods section for details on how the calculations are done.

REFERENCES

Ackerley, D., R. Chadwick, D. Dommenget, and P. Petrelli, 2018: An ensemble of AMIP simulations with prescribed land surface temperatures. *Geosci. Model Dev.*, **11**, 3865–3881, https://doi.org/10.5194/gmd-11-3865-2018.

Anagnostou, E., and Coauthors, 2016: Changing atmospheric CO_2 concentration was the primary driver of early Cenozoic climate. *Nature*, **533**, 380–384, https://doi.org/10.1038/nature17423.

——, and Coauthors, 2020: Proxy evidence for state-dependence of climate sensitivity in the Eocene greenhouse. *Nat. Commun.*, **11**, 4436, https://doi.org/10.1038/s41467-020-17887-x.

Andrews, T., C. J. Smith, G. Myhre, P. M. Forster, R. Chadwick, and D. Ackerley, 2021: Effective radiative forcing in a GCM with fixed surface temperatures. *J. Geophys. Res. Atmos.*, **126**, e2020JD033880, https://doi.org/10.1029/2020JD033880.

Bloch-Johnson, J., M. Rugenstein, M. B. Stolpe, T. Rohrschneider, Y. Zheng, and J. M. Gregory, 2021: Climate sensitivity increases under higher CO_2 levels due to feedback temperature dependence. *Geophys. Res. Lett.*, **48**, e2020GL089074, https://doi.org/10.1029/2020GL089074.

Block, K., and T. Mauritsen, 2013: Forcing and feedback in the MPI-ESM-LR coupled model under abruptly quadrupled CO_2. *J. Adv. Model. Earth Syst.*, **5**, 676–691, https://doi.org/10.1002/jame.20041.

Byrne, B., and C. Goldblatt, 2014: Radiative forcing at high concentrations of well-mixed greenhouse gases. *Geophys. Res. Lett.*, **41**, 152–160, https://doi.org/10.1002/2013GL058456.

Caballero, R., and M. Huber, 2013: State-dependent climate sensitivity in past warm climates and its implications for future climate projections. *Proc. Natl. Acad. Sci. USA*, **110**, 14 162–14 167, https://doi.org/10.1073/pnas.1303365110.

Chen, Y.-T., Y. Huang, and T. M. Merlis, 2023: The global patterns of instantaneous CO_2 forcing at the top of the atmosphere and the surface. *J. Climate*, **36**, 6331–6347, https://doi.org/10.1175/JCLI-D-22-0708.1.

——, T. M. Merlis, and Y. Huang, 2024: The cause of negative CO_2 forcing at the top-of-atmosphere: The role of stratospheric versus tropospheric temperature inversions. *Geophys. Res. Lett.*, **51**, e2023GL106433, https://doi.org/10.1029/2023GL106433.

Colman, R., and B. McAvaney, 2009: Climate feedbacks under a very broad range of forcing. *Geophys. Res. Lett.*, **36**, L01702, https://doi.org/10.1029/2008GL036268.

Dacie, S., and Coauthors, 2019: A 1D RCE study of factors affecting the tropical tropopause layer and surface climate. *J. Climate*, **32**, 6769–6782, https://doi.org/10.1175/JCLI-D-18-0778.1.

Edwards, J. M., and A. Slingo, 1996: Studies with a flexible new radiation code. I: Choosing a configuration for a large-scale model. *Quart. J. Roy. Meteor. Soc.*, **122**, 689–719, https://doi.org/10.1256/smsqj.53106.

Etminan, M., G. Myhre, E. J. Highwood, and K. P. Shine, 2016: Radiative forcing of carbon dioxide, methane, and nitrous oxide: A significant revision of the methane radiative forcing. *Geophys. Res. Lett.*, **43**, 12 614–12 623, https://doi.org/10.1002/2016GL071930.

Farnsworth, A., D. J. Lunt, C. L. O'Brien, G. L. Foster, G. N. Inglis, P. Markwick, R. D. Pancost, and S. A. Robinson, 2019: Climate sensitivity on geological timescales controlled by nonlinear feedbacks and ocean circulation. *Geophys. Res. Lett.*, **46**, 9880–9889, https://doi.org/10.1029/2019GL083574.

Forster, P. M., and Coauthors, 2016: Recommendations for diagnosing effective radiative forcing from climate models for CMIP6. *J. Geophys. Res. Atmos.*, **121**, 12 460–12 475, https://doi.org/10.1002/2016JD025320.

Friedrich, T., A. Timmermann, M. Tigchelaar, O. Elison Timm, and A. Ganopolski, 2016: Nonlinear climate sensitivity and its implications for future greenhouse warming. *Sci. Adv.*, **2**, e1501923, https://doi.org/10.1126/sciadv.1501923.

Hansen, J., and Coauthors, 2005: Efficacy of climate forcings. *J. Geophys. Res.*, **110**, D18104, https://doi.org/10.1029/2005JD005776.

Hartmann, D. L., 2015: *Global Physical Climatology*. International Geophysics Series, Vol. 56, Academic Press, 498 pp.

He, H., R. J. Kramer, B. J. Soden, and N. Jeevanjee, 2023: State dependence of CO_2 forcing and its implications for climate sensitivity. *Science*, **382**, 1051–1056, https://doi.org/10.1126/science.abq6872.

Huang, Y., X. Tan, and Y. Xia, 2016: Inhomogeneous radiative forcing of homogeneous greenhouse gases. *J. Geophys. Res. Atmos.*, **121**, 2780–2789, https://doi.org/10.1002/2015JD024569.

——, Y. Xia, and X. Tan, 2017: On the pattern of CO_2 radiative forcing and poleward energy transport. *J. Geophys. Res. Atmos.*, **122**, 10 578–10 593, https://doi.org/10.1002/2017JD027221.

Iacono, M. J., J. S. Delamere, E. J. Mlawer, M. W. Shephard, S. A. Clough, and W. D. Collins, 2008: Radiative forcing by long-lived greenhouse gases: Calculations with the AER radiative transfer models. *J. Geophys. Res.*, **113**, D13103, https://doi.org/10.1029/2008JD009944.

Jeevanjee, N., J. T. Seeley, D. Paynter, and S. Fueglistaler, 2021: An Analytical model for spatially varying clear-sky CO_2 forcing. *J. Climate*, **34**, 9463–9480, https://doi.org/10.1175/JCLI-D-19-0756.1.

Jonko, A. K., K. M. Shell, B. M. Sanderson, and G. Danabasoglu, 2012: Climate feedbacks in CCSM3 under changing CO2 forcing. Part I: Adapting the linear radiative kernel technique to feedback calculations for a broad range of forcings. *J. Climate*, **25**, 5260–5272, https://doi.org/10.1175/JCLI-D-11-00524.1.

Kay, J. E., and Coauthors, 2015: The Community Earth System Model (CESM) large ensemble project: A community resource for studying climate change in the presence of internal climate variability. *Bull. Amer. Meteor. Soc.*, **96**, 1333–1349, https://doi.org/10.1175/BAMS-D-13-00255.1.

Kelley, M., and Coauthors, 2020: Giss-e2.1: Configurations and climatology. *J. Adv. Model. Earth Syst.*, **12**, e2019MS002025, https://doi.org/10.1029/2019MS002025.

Kluft, L., S. Dacie, S. A. Buehler, H. Schmidt, and B. Stevens, 2019: Re-examining the first climate models: Climate sensitivity of a modern radiative–convective equilibrium model. *J. Climate*, **32**, 8111–8125, https://doi.org/10.1175/JCLI-D-18-0774.1.

Manabe, S., and R. T. Wetherald, 1967: Thermal equilibrium of the atmosphere with a given distribution of relative humidity. *J. Atmos. Sci.*, **24**, 241–259, https://doi.org/10.1175/1520-0469(1967)024<0241:TEOTAW>2.0.CO;2.

Manners, J., J. M. Edwards, P. Hill, and J.-C. Thelen, 2015: SOCRATES (Suite Of Community RAdiative Transfer codes based on Edwards and Slingo) Technical Guide. Met Office, https://code.metoffice.gov.uk/trac/socrates.

Mauritsen, T., and Coauthors, 2019: Developments in the MPI-M Earth System Model version 1.2 (MPI-ESM1.2) and its response to increasing CO_2. *J. Adv. Model. Earth Syst.*, **11**, 998–1038, https://doi.org/10.1029/2018MS001400.

Meraner, K., T. Mauritsen, and A. Voigt, 2013: Robust increase in equilibrium climate sensitivity under global warming. *Geophys. Res. Lett.*, **40**, 5944–5948, https://doi.org/10.1002/2013GL058118.

Miller, R. L., and Coauthors, 2021: CMIP6 historical simulations (1850–2014) with GISS-E2.1. *J. Adv. Model. Earth Syst.*, **13**, e2019MS002034, https://doi.org/10.1029/2019MS002034.

Mitevski, I., C. Orbe, R. Chemke, L. Nazarenko, and L. M. Polvani, 2021: Non-monotonic response of the climate system to abrupt CO_2 forcing. *Geophys. Res. Lett.*, **48**, e2020GL090861, https://doi.org/10.1029/2020GL090861.

——, L. M. Polvani, and C. Orbe, 2022: Asymmetric warming/cooling response to CO_2 increase/decrease mainly due to non-logarithmic forcing, not feedbacks. *Geophys. Res. Lett.*, **49**, e2021GL097133, https://doi.org/10.1029/2021GL097133.

——, Y. Dong, L. M. Polvani, M. Rugenstein, and C. Orbe, 2023: Non-monotonic feedback dependence under abrupt CO_2 forcing due to a North Atlantic pattern effect. *Geophys. Res. Lett.*, **50**, e2023GL103617, https://doi.org/10.1029/2023GL103617.

Mlynczak, M. G., and Coauthors, 2016: The spectroscopic foundation of radiative forcing of climate by carbon dioxide. *Geophys. Res. Lett.*, **43**, 5318–5325, https://doi.org/10.1002/2016GL068837.

Pincus, R., and Coauthors, 2020: Benchmark calculations of radiative forcing by greenhouse gases. *J. Geophys. Res. Atmos.*, **125**, e2020JD033483, https://doi.org/10.1029/2020JD033483.

Ramaswamy, V., M. D. Schwarzkopf, W. J. Randel, B. D. Santer, B. J. Soden, and G. L. Stenchikov, 2006: Anthropogenic and natural influences in the evolution of lower stratospheric cooling. *Science*, **311**, 1138–1141, https://doi.org/10.1126/science.1122587.

——, and Coauthors, 2018: Radiative forcing of climate: The historical evolution of the radiative forcing concept, the forcing agents and their quantification, and applications. *A Century of Progress in Atmospheric and Related Sciences: Celebrating the American Meteorological Society Centennial*, *Meteor. Monogr.*, No. 59, Amer. Meteor. Soc., https://doi.org/10.1175/AMSMONOGRAPHS-D-19-0001.1.

Richardson, T. B., and Coauthors, 2019: Efficacy of climate forcings in PDRMIP models. *J. Geophys. Res. Atmos.*, **124**, 12 824–12 844, https://doi.org/10.1029/2019JD030581.

Shaffer, G., M. Huber, R. Rondanelli, and J. O. Pepke Pedersen, 2016: Deep time evidence for climate sensitivity increase with warming. *Geophys. Res. Lett.*, **43**, 6538–6545, https://doi.org/10.1002/2016GL069243.

Sherwood, S. C., S. Bony, O. Boucher, C. Bretherton, P. M. Forster, J. M. Gregory, and B. Stevens, 2015: Adjustments in the forcing-feedback framework for understanding climate change. *Bull. Amer. Meteor. Soc.*, **96**, 217–228, https://doi.org/10.1175/BAMS-D-13-00167.1.

——, and Coauthors, 2020: An assessment of Earth's climate sensitivity using multiple lines of evidence. *Rev. Geophys.*, **58**, e2019RG000678, https://doi.org/10.1029/2019RG000678.

Smith, C. J., and Coauthors, 2018: Understanding rapid adjustments to diverse forcing agents. *Geophys. Res. Lett.*, **45**, 12 023–12 031, https://doi.org/10.1029/2018GL079826.

——, and Coauthors, 2020a: Effective radiative forcing and adjustments in CMIP6 models. *Atmos. Chem. Phys.*, **20**, 9591–9618, https://doi.org/10.5194/acp-20-9591-2020.

——, R. J. Kramer, and A. Sima, 2020b: The HadGEM3-GA7.1 radiative kernel: The importance of a well-resolved stratosphere. *Earth Syst. Sci. Data*, **12**, 2157–2168, https://doi.org/10.5194/essd-12-2157-2020.

Soden, B. J., I. M. Held, R. Colman, K. M. Shell, J. T. Kiehl, and C. A. Shields, 2008: Quantifying climate feedbacks using radiative kernels. *J. Climate*, **21**, 3504–3520, https://doi.org/10.1175/2007JCLI2110.1.

Wang, Y., and Y. Huang, 2020: Understanding the atmospheric temperature adjustment to CO_2 perturbation at the process level. *J. Climate*, **33**, 787–803, https://doi.org/10.1175/JCLI-D-19-0032.1.

Zhu, J., and C. J. Poulsen, 2020: On the increase of climate sensitivity and cloud feedback with warming in the community atmosphere models. *Geophys. Res. Lett.*, **47**, e2020GL089143, https://doi.org/10.1029/2020GL089143.

——, ——, and J. E. Tierney, 2019: Simulation of Eocene extreme warmth and high climate sensitivity through cloud feedbacks. *Sci. Adv.*, **5**, eaax1874, https://doi.org/10.1126/sciadv.aax1874.